

Advances in Understanding Top-of-Atmosphere Radiation Variability from Satellite Observations

Norman G. Loeb · Seiji Kato · Wenying Su · Takmeng Wong ·
Fred G. Rose · David R. Doelling · Joel R. Norris · Xianglei Huang

Received: 23 May 2011 / Accepted: 3 January 2012 / Published online: 27 January 2012
© The Author(s) 2012. This article is published with open access at Springerlink.com

Abstract This paper highlights how the emerging record of satellite observations from the Earth Observation System (EOS) and A-Train constellation are advancing our ability to more completely document and understand the underlying processes associated with variations in the Earth's top-of-atmosphere (TOA) radiation budget. Large-scale TOA radiation changes during the past decade are observed to be within 0.5 Wm^{-2} per decade based upon comparisons between Clouds and the Earth's Radiant Energy System (CERES) instruments aboard Terra and Aqua and other instruments. Tropical variations in emitted outgoing longwave (LW) radiation are found to closely track changes in the El Niño–Southern Oscillation (ENSO). During positive ENSO phase (El Niño), outgoing LW radiation increases, and decreases during the negative ENSO phase (La Niña). The coldest year during the last decade occurred in 2008, during which strong La Niña conditions persisted throughout most of the year. Atmospheric Infrared Sounder (AIRS) observations show that the lower temperatures extended throughout much of the troposphere for several months, resulting in a reduction in outgoing LW radiation and an increase in net incoming radiation. At the global scale, outgoing LW flux anomalies are partially compensated for by decreases in midlatitude cloud fraction and cloud height, as observed by Moderate Resolution Imaging Spectrometer and Multi-angle Imaging SpectroRadiometer, respectively. CERES data show that clouds have a net radiative warming influence during La Niña conditions and a net cooling influence during El Niño, but the magnitude of the anomalies varies greatly from one ENSO event to another. Regional cloud-radiation variations among several Terra and A-Train instruments show consistent patterns and

N. G. Loeb (✉) · S. Kato · T. Wong · D. R. Doelling
NASA Langley Research Center, Mail Stop 420, Hampton, VA 23681, USA
e-mail: norman.g.loeb@nasa.gov

W. Su · F. G. Rose
Science Systems and Applications, Inc., Hampton, VA 23666, USA

J. R. Norris
Scripps Institution of Oceanography, San Diego, CA 92037, USA

X. Huang
University of Michigan, Ann Arbor, MI 48109, USA

exhibit marked fluctuations at monthly timescales in response to tropical atmosphere-ocean dynamical processes associated with ENSO and Madden-Julian Oscillation.

Keywords Radiation budget · Clouds · Climate variability

1 Introduction

The top-of-atmosphere (TOA) Earth radiation budget (ERB) is determined from the difference between how much energy is absorbed and emitted by the planet. Climate forcing results in an imbalance in the TOA radiation budget that has direct implications for global climate, but the large natural variability in the Earth's radiation budget due to fluctuations in atmospheric and ocean dynamics complicates this picture. An illustration of the variability in TOA radiation is provided in Fig. 1, which shows a continuous 31-year record of tropical (20°S–20°N) TOA broadband outgoing longwave (LW) radiation (OLR) between 1979 and 2010 from non-scanner and scanner instruments. Figure 1a is an update to earlier

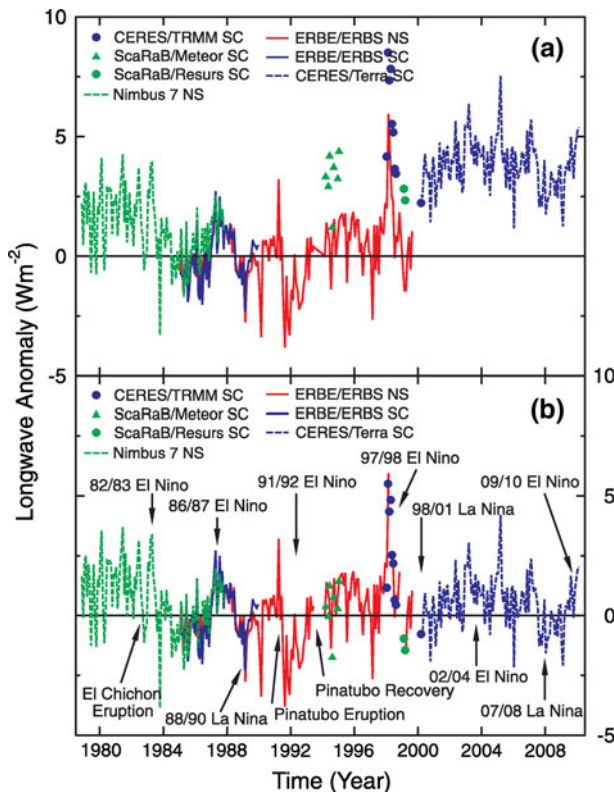


Fig. 1 LW TOA flux anomalies for 20°S–20°N from November 1978 to February 2010 **a** with no overlap correction, and **b** with overlap correction based upon ERBS Non-scanner WFOV Edition3_Rev1 (red solid line), Nimbus-7 Non-scanner (green dashed line), ERBS Scanner (blue solid line), CERES Terra crosstrack SSF1deg-lite_Ed2.5 (blue dashed line), CERES/TRMM Scanner Edition2 (blue circle), ScaRaB/Meteor Scanner (green triangle) and ScaRaB/Resurs Scanner (green circle). Anomalies are defined with respect to the 1985–1989 period

versions by Wielicki et al. (2002) and Wong et al. (2006). It shows rather marked jumps of up to 3 Wm^{-2} among the different satellites owing to absolute calibration differences, which are within measurement uncertainty. Because there is an overlap, the entire record can be placed on a common radiometric scale (Fig. 1b). Anomalies of up to 5 Wm^{-2} are observed during major El Niño–Southern Oscillation (ENSO; Philander 1990) events such as the 1997/98 El Niño. The record also provides quantitative data on the LW effect of the Pinatubo eruption and subsequent recovery.

With the availability of multiple years of data from new and improved passive instruments launched as part of the Earth Observing System (EOS) and active instruments belonging to the A-Train constellation (L'Ecuyer and Jiang 2010), a more complete observational record of ERB variations and the underlying processes is now possible. For the first time, simultaneous global observations of the ERB and a multitude of cloud, aerosol, and surface properties and atmospheric state data are available with a high degree of precision. These data are a far more comprehensive set for evaluating climate model simulations compared to ERB observations alone (Wielicki et al. 2002).

This study analyzes ERB observations from the Clouds and the Earth's Radiant Energy System (CERES) aboard Terra and Aqua together with data from several other instruments on Terra, Aqua and A-Train. We first examine how consistently independent satellite instruments observe large-scale (tropical and global) changes in radiation budget during the past decade. Next, we explore the relationship between large-scale outgoing SW and LW TOA radiative flux variations and ENSO and relate the TOA flux variations to cloud property variations. Finally, we illustrate how the new generation of satellite observations collectively enables a far more detailed description of the regional response of clouds and radiation to circulation changes associated with ENSO and Madden–Julian Oscillation (MJO; Madden and Julian 1971, 1994).

2 CERES Observations

This study uses 10 years (March 2000–February 2010) of CERES Terra and 7 years 8 months (July 2002–February 2010) of CERES Aqua regional monthly mean data from the CERES SSF1deg-lite_Ed2.5 data product. CERES SSF1deg-lite_Ed2.5 provides CERES TOA radiative fluxes and coincident cloud and aerosol properties from the Moderate Resolution Imaging Spectroradiometer (MODIS) (Salomonson et al. 1989; Barnes et al. 1998). Cloud retrievals are based upon Minnis et al. (2011), while aerosol data are from Remer et al. (2005). Each parameter is available at 1° -regional, zonal and global time–space scales. TOA fluxes are provided for clear and all-sky conditions in the long-wave (LW), shortwave (SW), and window (WN) regions (Loeb et al. 2005). Net incoming TOA flux is determined from the difference between the observed TOA incoming solar irradiance and the sum of the outgoing reflected solar and emitted LW radiation. TOA solar irradiance is based upon time-varying observations from the Solar Radiation and Climate Experiment (SORCE; Woods et al. 2000) mission, which are updated daily (SORCE Level 3 Total Solar Irradiance Version 10 available from: http://lasp.colorado.edu/sorce/data/tsi_data.htm).

Regional mean TOA fluxes for 1° equal-area grid boxes in the CERES SSF1deg-Ed2.5 data product are interpolated using the assumption of constant meteorological conditions (termed non-geostationary or non-GEO) similar to the process used to average CERES ERBE-like data (Young et al. 1998). In the SW, TOA fluxes between observation times are interpolated, taking into account TOA solar irradiance changes throughout the day and the

albedo dependence on solar zenith angle for the scene observed at the CERES observation time. To interpolate LW TOA flux for cloud-free scenes over land, CERES SSF1deg-lite applies a half-sine fit to approximate the diurnal cycle of OLR (Young et al. 1998). Otherwise, only the available daytime and nighttime LW observations are used to determine a daily mean. After interpolation, the time series is used to produce monthly means, calculated using the combination of observed and interpolated parameters from all days containing at least one CERES observation (Doelling et al. 2012).

A cloud mask (Minnis et al. 2011) is applied to MODIS 1-km pixels within CERES footprints to identify scenes that are clear and cloudy. Clear-sky TOA fluxes are determined from CERES footprints for which 99.9% or more of the MODIS pixels within the CERES footprint are identified as cloud-free. This study also uses clear-sky TOA fluxes from the recently released Energy Balanced and Filled (EBAF) Edition2.5A for March 2000–February 2010. Because of the coarse spatial resolution of CERES (20 km at nadir), clear-sky TOA fluxes in SSF1deg-lite_Ed2.5 only include contributions from cloud-free regions occurring over relatively large spatial scales and meteorological conditions and geographical regions where clouds occur less frequently. In EBAF, clear-sky TOA flux contributions at smaller spatial scales are recovered by inferring broadband TOA fluxes from MODIS radiances in clear portions of partly cloudy CERES footprints. The methodology, described in Loeb et al. (2009), involves using MODIS-CERES narrow-to-broadband regressions to convert MODIS narrowband radiances averaged over the clear portions of a footprint to broadband radiances. The “broadband” MODIS radiances are then converted to TOA radiative fluxes using CERES clear-sky Angular Distribution Models (Loeb et al. 2005).

Another advance in CERES SSF1deg-lite_Ed2.5 is that it includes the latest CERES instrument calibration improvements. The CERES team reanalyzed ground and in-flight calibration data and implemented a new algorithm to characterize the spectral degradation of the CERES optics with time that, if left uncorrected, leads to a decrease in SW radiances and a day/night inconsistency in LW radiances. A summary of the instrument calibration improvements required to overcome these problems is provided in Appendix 1.

3 Results

3.1 Comparison of TOA Radiation Variability from Different Instruments

Tropical (30°S–30°N) and global deseasonalized monthly anomalies of outgoing SW and LW and incoming net radiation from CERES Terra for March 2000–February 2010 and CERES Aqua for July 2002–February 2010 are provided in Fig. 2 and summarized in Table 1. A deseasonalized monthly anomaly is determined by differencing the average in a given month from the average of all years of the same month. As expected, variability is greater in the tropics than for the globe. Pronounced positive net TOA flux anomalies in 2008 are clearly evident in Fig. 2e, f. This period is characterized by 22 consecutive months of negative outgoing LW TOA flux anomalies in the tropics (between June 2007 and March 2009), and negative outgoing SW TOA flux anomalies in both the tropics and globally during much of 2008 and early 2009. The minimum tropical outgoing LW TOA flux anomaly occurs in January 2008, the coldest of all Januaries during the CERES Terra record. The peak net incoming TOA flux anomaly occurs in June 2009, shortly after the transition from La Nina to El Nino conditions, and reaches 2.5 Wm^{-2} in the tropics and 1.5 Wm^{-2} globally.

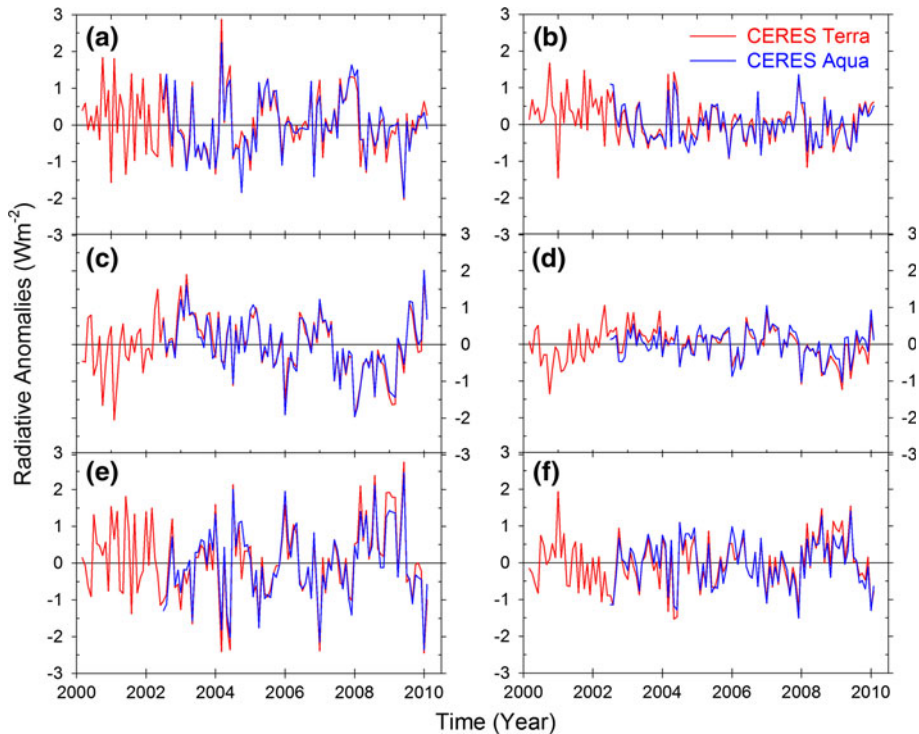


Fig. 2 CERES Terra and Aqua deseasonalized monthly for SW (a and b), LW (c and d), Net (e and f) TOA radiation. *Left column* corresponds to 30°S–30°N and *right column* corresponds to global. The CERES Terra record is from March 2000–February 2010, and the CERES Aqua record is from July 2002–February 2010. Both Terra and Aqua records use their respective means for July 2002–February 2010 to compute the anomalies

When CERES Terra and CERES Aqua are compared for July 2002 through February 2010 (Fig. 3; Table 1), differences are generally much smaller than the variability, as evident from the coefficient of determination (r^2) values, which exceed 0.92 in the tropics, and 0.81 globally (Table 1). Differences in SW trends between the two records are generally smaller than 0.3 W m^{-2} per decade. For global LW, CERES Terra shows a 0.63 W m^{-2} per decade steeper increase than CERES Aqua. The cause for the drift between Terra and Aqua LW TOA fluxes is due to an artificial discontinuity in the middle of the Aqua record that will be corrected for in the next release (see Appendix 2 for more details).

The CERES data record also shows excellent agreement with data records from other instruments. This is illustrated in Fig. 4a–c and Table 2. Figure 4a compares the stability of the CERES Terra SW observations with anomalies in Photosynthetically Active Radiation (PAR) from the Sea-Viewing Wide-Field-of-View Sensor (SeaWiFS; Hooker et al. 1992) (2009 reprocessing), launched in August 1997 onboard the SeaStar spacecraft. A detailed description of the methodology used in the comparison is provided in Loeb et al. (2007). Briefly, deseasonalized CERES SW TOA flux anomalies for all-sky ocean between 30°S and 30°N from the CERES Terra SSF1deg-lite_Ed2.5 data product are plotted against deseasonalized anomalies in SeaWiFS PAR. The SeaWiFS PAR anomalies are then multiplied by the slope of the regression line (-6.09 W m^{-2} per $\text{E m}^{-2} \text{ day}^{-1}$) in order to

Table 1 Statistical summary tropical (30°S–30°N) and global CERES Terra deseasonalized monthly anomalies for SW, LW and net TOA radiation from July 2002–February 2010 for CERES Terra and CERES Aqua SSF1deg-lite_Ed2.5 and their difference (“Diff”)

	30°S–30°N					Global				
	σ	m	ε	δ	r^2	σ	m	ε	δ	r^2
SW										
Terra	0.82	−0.03	0.94	–	–	0.52	0.00	0.51	–	–
Aqua	0.78	0.02	0.98	–	–	0.49	−0.11	0.53	–	–
Diff	0.23	0.04	0.27	0.27	0.92	0.18	−0.12	0.25	0.27	0.89
LW										
Terra	0.79	−1.30	1.27	–	–	0.43	−0.82	0.56	–	–
Aqua	0.78	−0.90	1.23	–	–	0.40	−0.19	0.49	–	–
Diff	0.18	0.39	0.21	0.45	0.95	0.19	0.63	0.36	0.72	0.81
Net										
Terra	1.06	1.00	1.36	–	–	0.67	0.55	0.77	–	–
Aqua	0.97	0.56	1.26	–	–	0.64	0.04	0.76	–	–
Diff	0.28	−0.44	0.37	0.58	0.93	0.23	−0.51	0.39	0.64	0.88
WN										
Terra	0.34	−0.59	0.61	–	–	0.17	−0.34	0.23	–	–
Aqua	0.32	−0.19	0.51	–	–	0.16	−0.04	0.22	–	–
Diff	0.13	0.4	0.31	0.5	0.86	0.09	0.3	0.27	0.4	0.68

σ , Standard deviation of monthly anomalies (Wm^{-2}); m , slope of linear regression fit to monthly anomalies (Wm^{-2} per decade); ε , 95% confidence in m (Wm^{-2} per decade); $\delta = (m^2 + \varepsilon^2)^{1/2}$ (Wm^{-2} per decade), r^2 , coefficient of determination

place the two records on the same radiometric scale. Results show agreement in monthly anomalies to 0.29 Wm^{-2} , and agreement in the overall slope to $<0.4 \text{ Wm}^{-2}$ per decade at the 95% confidence level for all data through the end of 2008. In early 2008, SeaStar spacecraft anomalies caused significant reductions in sampling, resulting in a much noisier comparison.

A comparison of tropical CERES Terra SW TOA flux and MODIS Terra cloud fraction anomalies (Fig. 4b) shows a slightly negative change over the decade (Table 2) within their respective 95% confidence intervals, and the r^2 between these variables is 0.82. Figure 4c compares CERES Terra and Aqua LW TOA flux anomalies with Atmospheric Infrared Sounder (AIRS) outgoing LW flux (monthly AIRX3STM.005 product) anomalies for 30°S–30°N from September 2002 and June 2009. AIRS TOA fluxes from ascending and descending orbits are linearly averaged without any correction for diurnal cycle effects. CERES SSF1deg-lite applies a half-sine fit over land to approximate the diurnal cycle of OLR (Young et al. 1998). The r^2 value exceeds 0.9 in both the AIRS/CERES Terra and AIRS/CERES Aqua comparisons (Table 2). Also, LW TOA flux anomalies are negative from mid-2007 through March 2009, and steadily increase thereafter in all three data records. Susskind et al. (2012) provide a more extensive AIRS-CERES analysis comparing regional and zonal LW TOA fluxes and find excellent agreement in the pattern of OLR anomaly trends between AIRS and CERES.

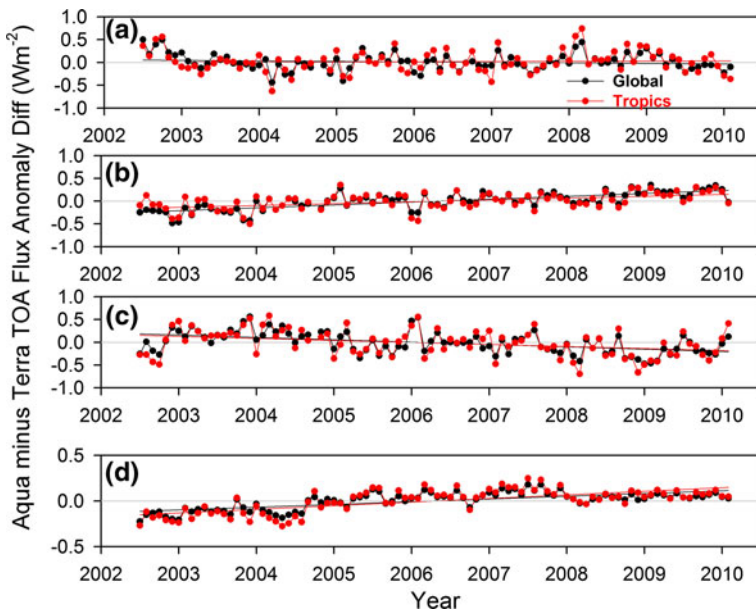


Fig. 3 Global and tropical (30°S–30°N) Aqua minus Terra CERES TOA flux anomaly difference for **a** SW, **b** LW, **c** Net and **d** WN for July 2002–February 2010

3.2 ENSO Influence on TOA Radiation Variability at Tropical and Global Scales

To explore the relationship between interannual variations in CERES TOA flux and ENSO, Fig. 5a shows outgoing LW TOA flux anomalies from CERES Terra with multivariate ENSO index (MEI; Wolter and Timlin 1998) for the tropics (30°S–30°N) and globe. The CERES TOA flux anomalies are smoothed with a 2-month running mean, consistent with MEI. In the tropics, there is a fairly good relationship between LW TOA flux anomalies and MEI, with an r^2 value of 0.56. Earlier studies (Allan and Singo 2002; Wong et al. 2006) showed a similar relationship between LW TOA flux and ENSO: for example, the 1997/98 El Niño resulted in monthly anomalies greater than 5 Wm^{-2} in the tropics. Positive MEI values (El Niño-like conditions) are associated with positive outgoing LW TOA flux anomalies, and negative MEI values (La Niña-like conditions) are associated with negative outgoing LW TOA flux anomalies. From mid-2007 through spring 2009, La Niña conditions dominate with two broad peaks in MEI occurring during the 2008 and 2009 winter seasons. Both of these events are associated with negative peaks in outgoing LW TOA flux anomalies, reaching -1.5 Wm^{-2} , and a pronounced reduction in tropospheric temperatures, as observed by AIRS (Fig. 6a). Anomalies in water vapor mixing ratio (Fig. 6b) are negative in the lower troposphere up to 600 mb through mid-2008, and become positive thereafter.

Globally, the relationship between outgoing LW TOA flux anomalies and MEI is much weaker ($r^2 = 0.25$), but there is still a tendency for negative LW TOA flux anomalies during extended periods of negative MEI. The pronounced minimum in tropical LW TOA flux anomaly in early 2008 is consistent with expectation: January 2008 was the coldest month in over a decade. Why then are the global average LW anomalies so much weaker than those in the tropics? It turns out that LW anomalies in the middle latitudes associated

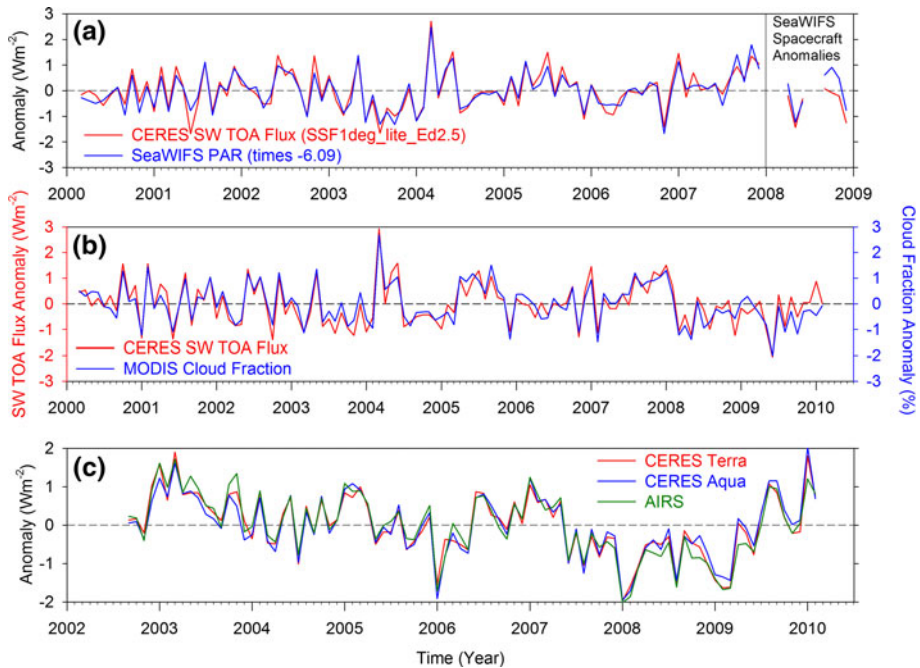


Fig. 4 Monthly anomalies in **a** CERES Terra SW TOA flux from SSF1deg-lite_Ed2.5 and SeaWiFS PAR scaled by a factor of -6.09 (corresponding to the slope of the regression line fit relating CERES SW TOA flux and SeaWiFS PAR anomalies) over ocean for 30°S – 30°N from March 2000 to December 2009, **b** CERES Terra SW TOA flux and MODIS cloud fraction for 30°S – 30°N between March 2000 and February 2010 and **c** global LW TOA flux from CERES Terra, CERES Aqua and AIRS Aqua for September 2002–February 2010

with large cloud property changes compensate for the decrease in outgoing LW radiation in the tropics. Figure 5b shows anomalies in midlatitude (30°S – 60°S and 30°N – 60°N) mean CERES LW TOA flux, MODIS cloud fraction, and Multi-angle Imaging SpectroRadiometer (MISR) cloud-top height. The MISR cloud-top height anomalies are determined from the MISR Cloud Fraction by Altitude product (Di Girolamo et al. 2010). During the 2007–2008 La Niña (yellow shaded region), midlatitude MODIS cloud fraction and MISR cloud-top height anomalies are both pronounced and negative. Since LW emission to space is greater in cloud-free regions and from clouds with lower tops, it follows that midlatitude LW TOA flux should increase, resulting in weaker global mean LW TOA flux anomalies. While it is plausible that the midlatitude cloud-radiation changes are related to circulation changes associated with the La Niña event in the tropics, other factors may also play a role.

To examine the role that clouds play in modulating tropical and global TOA flux variations, Fig. 7a–f compare all-sky and clear-sky outgoing SW and LW and net incoming TOA flux anomalies. Clear-sky TOA flux anomalies are based upon CERES TOA fluxes from cloud-free scenes, as identified from MODIS observations. We consider two sets of clear-sky TOA flux datasets. “Clear-sky (SSF1deg)” considers only CERES footprints in which 99.9% or more of the MODIS pixels within the CERES footprint are identified as cloud-free. “Clear-sky (EBAF)” is from the CERES Energy Balanced and Filled (CERES_EBAF_Edition2.5) Product (Loeb et al. 2009) and includes clear-sky TOA flux contributions from cloud-free regions in partly cloudy CERES footprints. In the SW,

Table 2 Same as Table 1 but for tropics (30°S–30°N)

	σ	m	ε	δ	r^2
<i>CERES Terra and SeaWIFS (03/2000–12/2008)</i>					
SW					
Terra	0.78	0.12	0.63	–	–
SeaWIFS	0.73	0.41	0.60	–	–
Diff	0.29	0.30	0.28	0.41	0.86
<i>CERES Terra and MODIS (03/2000–02/2010)</i>					
SW/f					
CERES SW	0.83	–0.25	0.55	–	–
MODIS f	0.77	–0.48	0.57	–	–
					0.82
<i>CERES Terra and AIRS (09/2002–06/2009)</i>					
LW					
CERES	0.79	–1.35	1.33	–	–
AIRS	0.83	–1.68	1.60	–	–
Diff	0.21	–0.33	0.22	0.40	0.93
<i>CERES Aqua and AIRS (09/2002–06/2009)</i>					
LW					
CERES	0.78	–0.93	1.29	–	–
AIRS	0.83	–1.68	1.60	–	–
Diff	0.25	–0.76	0.37	0.84	0.90

there is little correlation between clear and all-sky TOA fluxes. This is not surprising given the high correlation between CERES all-sky SW TOA flux and MODIS cloud fraction anomalies shown in Fig. 4b. However, in the LW, clear and all-sky TOA flux anomalies show very similar changes throughout the decade, both in the tropics and globally. During the 2008 La Niña, the magnitude of tropical clear-sky outgoing LW TOA flux anomalies is very similar to all-sky, consistent with the pronounced cooling throughout the troposphere during this period (Fig. 6a). In other parts of the LW record, clouds appear to introduce more high-frequency variations, as is evident from the abrupt spikes in the all-sky but not the clear-sky anomalies. As net incoming TOA flux is derived from both SW and LW contributions, the correlation between clear and all-sky net TOA flux is weaker, but nonetheless still apparent.

To compare the relative contribution of the surface, atmosphere and clouds on LW TOA flux variations, we use a plane-parallel radiative transfer code (Fu and Liou 1992, 1993) and perform a radiative perturbation analysis with observed variations in surface skin temperature (T_s) from the Global Modeling and Assimilation Office (GMAO)'s Goddard Earth Observing System (GEOS) Data Assimilation System (DAS) V4 (2003–2007) and V5 (2008–2009) products (Suarez 2005), atmospheric temperature ($T(z)$) and water vapor mixing ratio ($w(z)$) from AIRS, and effective cloud-top pressure (P_c), cloud fraction (f) and cloud optical depth (τ_c) from MODIS (Minnis et al. 2011). We set water vapor mixing ratio above 70 hPa to 10^{-6} g/g, and ozone is a fixed Midlatitude Summer standard atmosphere profile. The contribution to OLR variability by a given variable is computed from the difference between an OLR time series calculated using input variables specified by their monthly mean values for 84 months (January 2003–December 2009) and a second

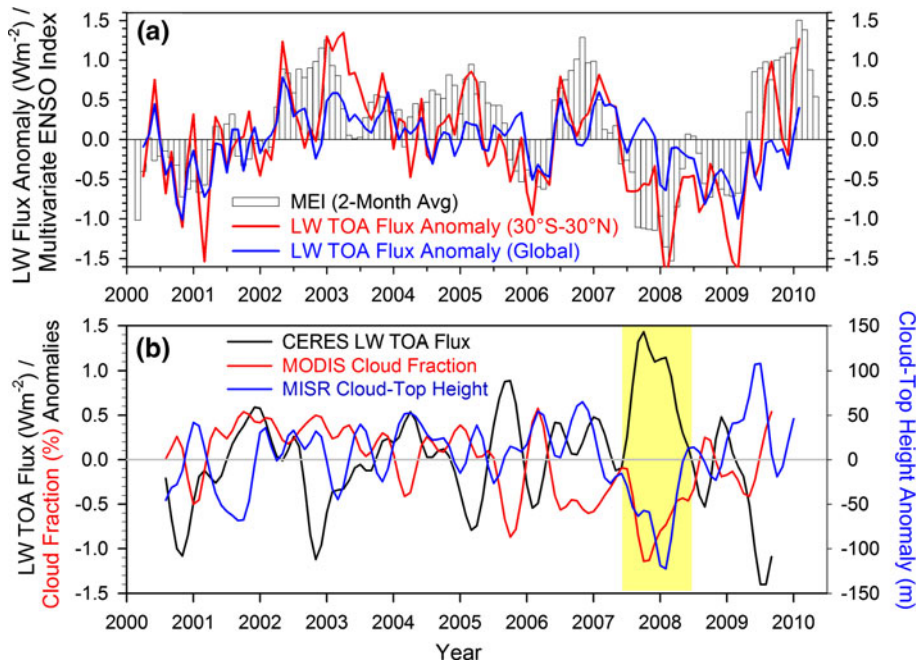


Fig. 5 **a** Deseasonalized anomalies in tropical (30°S – 30°N) and global CERES LW TOA flux together with the multivariate ENSO Index (MEI). A 2-month running average is used to determine the LW TOA flux anomalies. **b** Deseasonalized anomalies in midlatitude (30°S – 60°S and 30°N – 60°N) mean CERES LW TOA flux, MODIS cloud fraction and MISR cloud-top height. An 11-point 6-month low-pass Lanczos filter is applied to the monthly anomalies

calculation identical to the first but with the parameter in question held fixed at its climatological monthly mean values. The climatological monthly mean values of each input variable are determined using data from all Januaries, Februaries, etc., for 2003–2009 in each $1^{\circ} \times 1^{\circ}$ deg region. In order to quantify the combined influence of variations in atmospheric temperature and humidity on OLR variability, the same approach is used but holding both variables fixed at their climatological values when calculating the difference. Similarly, the impact of clouds is determined by computing the combined contribution to OLR variability by P_c , f and τ_c . As a simplification, we assume single-layer clouds in the calculations, with cloud-top pressure given by the observed cloud fraction-weighted mean cloud-top pressure in a gridbox. With this simplification, it is not possible to determine whether a cloud fraction change corresponds to a change in low or high cloud, nor can we ascribe a change in cloud-top pressure to a change in low or high cloud altitude.

Figure 8a–g show the results of this analysis for all-sky (left-hand column) and clear-sky (right-hand column) conditions in the tropics. When variations from all parameters are included (Fig. 8a, b), calculated OLR anomalies (black line) agree well with CERES (red line). Atmospheric ($T(z)$ and $w(z)$) contributions explain most of the clear-sky LW TOA flux variations (Fig. 8d), and while the surface temperature contribution is correlated with that of $T(z)$, it is only appreciable in magnitude in early 2008, during the peak of the 2007–2008 La Niña event. Atmospheric temperature and water vapor mixing ratio contributions to LW TOA flux variability are negatively correlated (Fig. 8e, f), with lower (drier) temperature (water vapor) changes during the cold phase of ENSO reducing

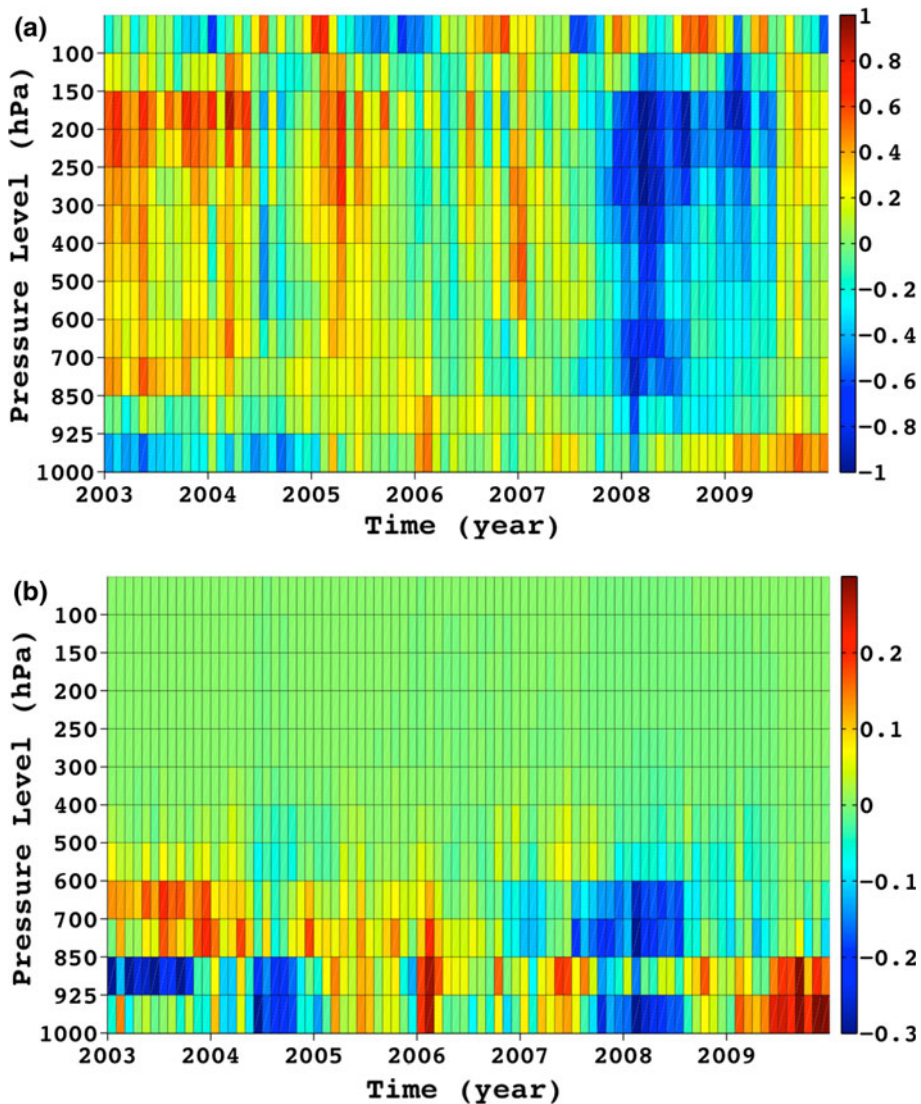


Fig. 6 AIRS low-latitude (30°S–30°N) temperature anomalies (K) as a function of pressure level

(enhancing) LW TOA flux. Overall, atmospheric temperature variations have a greater impact on LW TOA flux variability than water vapor changes. In all-sky conditions, atmosphere and cloud contributions generally track one another and contribute roughly equally to LW TOA flux variability. LW contributions by P_c and f are generally in phase with one another, particularly during stronger ENSO events.

A summary of tropical and global TOA flux anomalies averaged over intervals of positive and negative MEI is provided in Table 3. All tropical and most global mean LW Cloud Radiative Effect (CRE) anomalies are positive (enhanced radiative warming to the system) during La Niña events and negative (reduced radiative warming to the system) during El Niño events. The magnitude of LW cloud radiative anomalies in comparison to

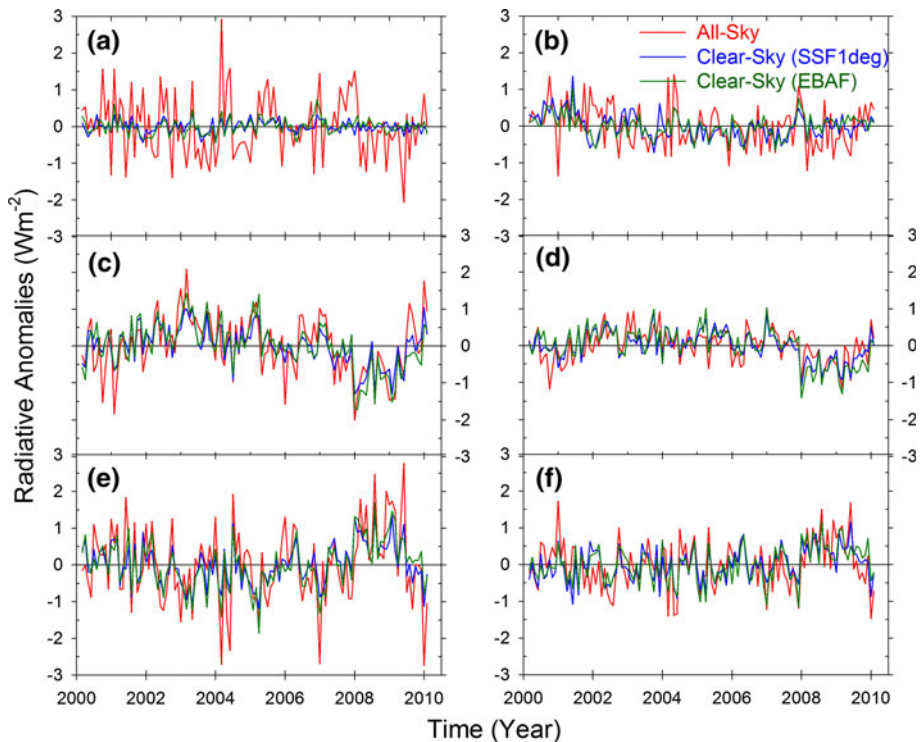


Fig. 7 CERES Terra deseasonalized monthly anomalies for SW (a and b), LW (c and d), Net (e and f) TOA radiation from March 2000–February 2010. *Left column* corresponds to 30°S–30°N and *right column* corresponds to global

clear-sky anomalies varies from one ENSO event to another, however. Average LW cloud radiative effects (CRE) are pronounced during the 03/00–03/02 La Niña event, as well as during the 05/06–05/07 and 05/09–02/10 El Niño events. In contrast, average LW CREs are relatively weak during the 06/07–04/09 La Niña and 04/02–09/05 El Niño events. Average clear-sky anomalies during the 06/07–04/09 La Niña are a factor of 2 larger than in any other ENSO interval during the decade.

Table 4 provides a summary of anomalies in cloud fraction, cloud-top pressure and visible cloud optical depth from MODIS. In two of the three El Niño events, mean cloud fraction anomalies are near-zero, and cloud-top pressure anomalies are positive. At the peak of the El Niño events (early 2003, 2005, 2007), LW flux contributions from cloud fraction and cloud-top pressure are both positive (Fig. 8g) (reducing LW CRE). During the 05/09–02/10 El Niño event, the decrease in LW CRE is associated with a sharp decline in cloud cover of -0.8% , which is partially compensated for by an increase in cloud-top height (Fig. 8g). Average cloud fraction anomalies are near-zero or positive during La Niña events (Table 4), and in 2 of the 3 events, moderate negative cloud-top pressure anomalies are observed.

In the tropics, SW CREs (Table 3) dominate over clear-sky radiative effects by at least a factor of 3, and SW CRE anomalies are positive in all 3 El Niño events and negative in 2 of the 3 La Niña events. The strongest El Niño event (05/09–02/10) is associated with the greatest change in both cloud fraction and cloud optical depth (both showing decreases)

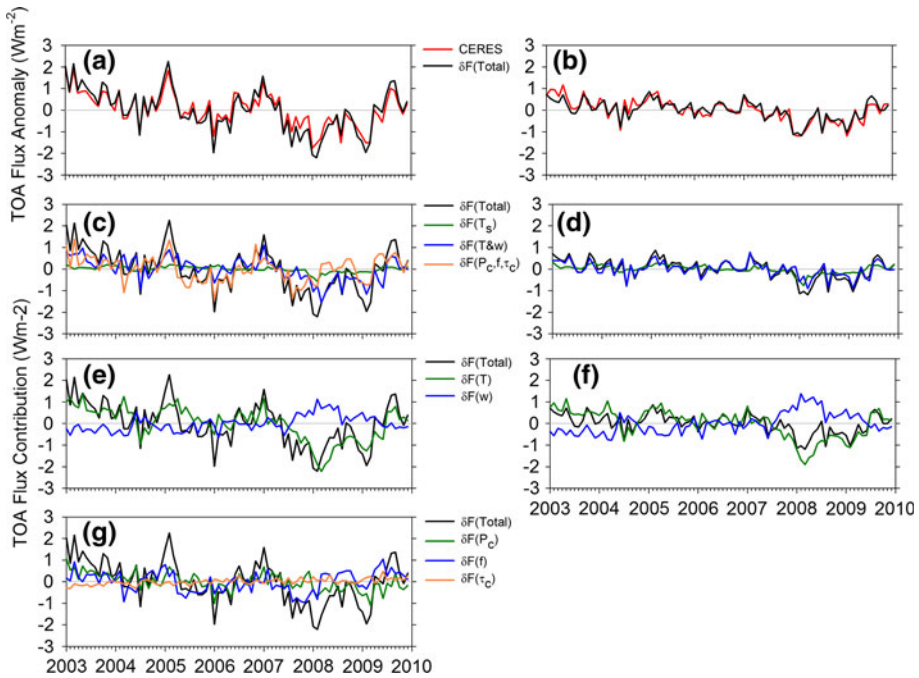


Fig. 8 CERES and calculated monthly anomalies in tropical mean LW TOA flux for **a** all-sky and **b** clear-sky; contribution to LW TOA flux from surface temperature ($dF(T_s)$), atmospheric temperature and humidity ($dF(T&w)$), clouds (P_c, f, t_c) for **c** all-sky and **d** clear-sky; contribution to LW TOA flux from T and w for **e** all-sky and **f** clear-sky; contribution to LW TOA flux from P_c, f and t_c

(Table 4). Average net CRE anomalies are near-zero in all but two ENSO events. During the 10/05–04/06 La Niña event, reduced SW cloud radiative cooling combined with enhanced LW CRE anomalies produce a net CRE of 0.39 Wm^{-2} . In contrast, during the 05/06–05/07 El Niño, the tropical net CRE anomaly reaches -0.34 Wm^{-2} due to a large negative LW CRE anomaly and a near-zero SW CRE. Thus, while the net radiative effect of clouds is that of warming (cooling) across the tropics during La Niña (El Niño) events, the magnitude is quite small and varies greatly from one event to another.

Results in Tables 3 and 4 are generally consistent with a recent study by Zelinka and Hartmann (2011) who used satellite observations to examine the relationship between tropical mean CRE and surface temperature anomalies. They find that LW CRE decreases with surface temperature, and SW CRE increases. This is consistent with negative (positive) LW CRE anomalies and positive (negative) SW CRE anomalies during El Niño (La Niña) (Table 3). Further, Zelinka and Hartmann (2011) show that while high clouds rise with warming, in agreement with the fixed anvil temperature (Hartmann and Larson 2002) and proportionately higher anvil temperature (Zelinka and Hartmann 2010) hypotheses, the increase is compensated by a decrease in high cloud amount. This is qualitatively consistent with a decrease (increase) in both cloud fraction and cloud-top pressure during El Niño (La Niña) (Table 4 and implied from Fig. 8g). Furthermore, the SW radiative cooling effect of clouds decreases in warmer conditions, owing to a decrease in tropical mean cloud fraction.

Results in the present study and Zelinka and Hartmann (2011) show a tendency for a negative LW and positive SW cloud feedback response to ENSO in the tropics. This is

Table 3 Summary of cloud and clear-sky radiative effect by MEI interval (Wm^{-2})

Date	MEI	SW (All)	SW (Clr)	SW CRE	LW (All)	LW (Clr)	LW CRE	NET (All)	NET (Clr)	NET CRE
Tropics (30°S–30°N)										
03/00–03/02	−0.25	0.18	−0.02	−0.21	−0.21	0.06	0.27	0.22	0.16	0.06
04/02–09/05	0.55	−0.04	0.02	0.06	0.40	0.32	−0.08	−0.33	−0.32	−0.01
10/05–04/06	−0.46	−0.15	0.03	0.19	−0.38	−0.18	0.20	0.47	0.08	0.39
05/06–05/07	0.61	−0.03	0.02	0.05	0.40	0.01	−0.39	−0.44	−0.10	−0.34
06/07–04/09	−0.67	0.06	−0.02	−0.08	−0.78	−0.61	0.16	0.56	0.48	0.08
05/09–02/10	0.96	−0.28	−0.05	0.23	0.38	0.04	−0.34	−0.21	−0.10	−0.11
Global										
03/00–03/02	−0.25	0.32	0.24	−0.09	−0.18	0.04	0.21	0.03	−0.10	0.13
04/02–09/05	0.55	−0.04	−0.02	0.02	0.21	0.20	−0.01	−0.15	−0.16	0.00
10/05–04/06	−0.46	−0.18	−0.26	−0.07	−0.07	0.13	0.20	0.20	0.07	0.13
05/06–05/07	0.61	−0.21	−0.16	0.04	0.27	0.11	−0.16	−0.14	−0.02	−0.11
06/07–04/09	−0.67	−0.14	−0.05	0.10	−0.28	−0.40	−0.12	0.30	0.32	−0.02
05/09–02/10	0.96	0.08	0.00	−0.08	−0.10	−0.24	−0.14	−0.07	0.14	−0.21

Each value corresponds to the mean anomaly for the indicated time period. *Bold values* exceed the standard error in the mean

Table 4 Summary of tropical mean (30°S–30°N) cloud property changes by MEI interval

Date	MEI	Cloud fraction (%)	Cloud-top pressure (hPa)	Cloud optical depth
03/00–03/02	−0.25	0.095	1.4	0.041
04/02–09/05	0.55	0.03	1.5	0.026
10/05–04/06	−0.46	0.38	−4.2	−0.013
05/06–05/07	0.61	0.13	1.7	−0.034
06/07–04/09	−0.67	0.00	−3.1	−0.020
05/09–02/10	0.96	−0.80	−1.8	−0.11

Each value corresponds to the mean anomaly for the indicated time period. *Bold values* exceed the standard error in the mean

consistent with Lin et al. (2002) based upon CERES Tropical Rainfall Measurement Mission (TRMM) data. Trenberth et al. (2010) find the overall feedback to be positive in the tropics. Globally, Dessler (2010) finds positive cloud feedbacks both for SW and LW after accounting for changes in clear-sky SW and LW properties masked by clouds. Positive SW cloud feedback is also observed in Clement et al. (2009) and Eitzen et al. (2011), who focused on marine boundary layer regimes.

3.3 ENSO Influence on TOA Radiation Variability Regional Scales

The regional pattern of TOA radiation, cloud property and skin temperature anomalies during the first 2 months of 2008 at the height of the 2008 La Niña event are provided in Figs. 9 and 10. During this period, negative SST anomalies persist across the equatorial Pacific basin, consistent with expectation during a La Niña event. Negative SST anomalies

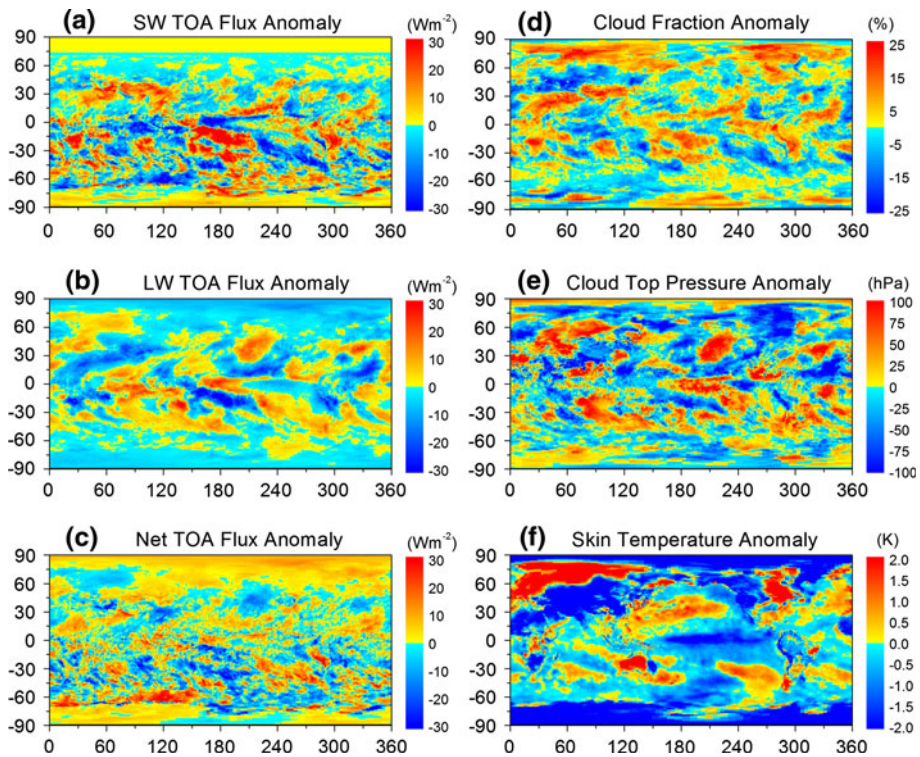


Fig. 9 Regional anomalies (relative to March 2000–February 2010 climatology) for January 2008. **a** SW TOA flux; **b** LW TOA flux; **c** net TOA flux; **d** cloud fraction; **e** cloud-top pressure; **f** skin temperature

are also found along the west coasts of the Americas, and positive anomalies occur in the west and central Pacific Ocean between 30°N and 45°N . This pattern is consistent with a negative Pacific Decadal Oscillation (PDO) pattern—in fact, 2008 saw the lowest PDO index since 1971 (Xue and Reynolds 2009). Regional patterns of CERES SW (Figs. 9a, 10a) and LW (Figs. 9b, 10b) TOA flux anomalies are closely linked to patterns of MODIS cloud fraction (Figs. 9d, 10d) and cloud-top pressure (Figs. 9e, 10e), respectively. Positive anomalies in cloud fraction and negative anomalies in cloud-top pressure likely due to stronger than normal low-level convergence in the South Pacific Convergence Zone (SPCZ) are associated with positive anomalies in reflected SW TOA flux and negative anomalies in LW TOA flux, respectively. In the North Pacific and Atlantic Oceans between 30°N and 60°N in January (Fig. 9), large areas of positive cloud-top pressure anomalies are closely tied to positive anomalies in LW TOA flux. Because SW TOA flux anomalies associated with these features are weak, these features show up quite clearly as areas of negative net TOA flux anomalies in Fig. 9c. Otherwise, with the exception of a few areas of extensive negative net TOA flux anomalies in the Southern Oceans associated with positive cloud fraction anomalies, most of the globe shows weak positive net TOA flux anomalies.

There is a striking difference between the January and February 2008 regional pattern of cloud property and TOA radiation anomalies. In February, a pronounced dipole pattern appears in which negative outgoing LW (positive SW) TOA flux anomalies occur over the Indian Ocean extending eastward to Indonesia and over the SPCZ, and positive outgoing

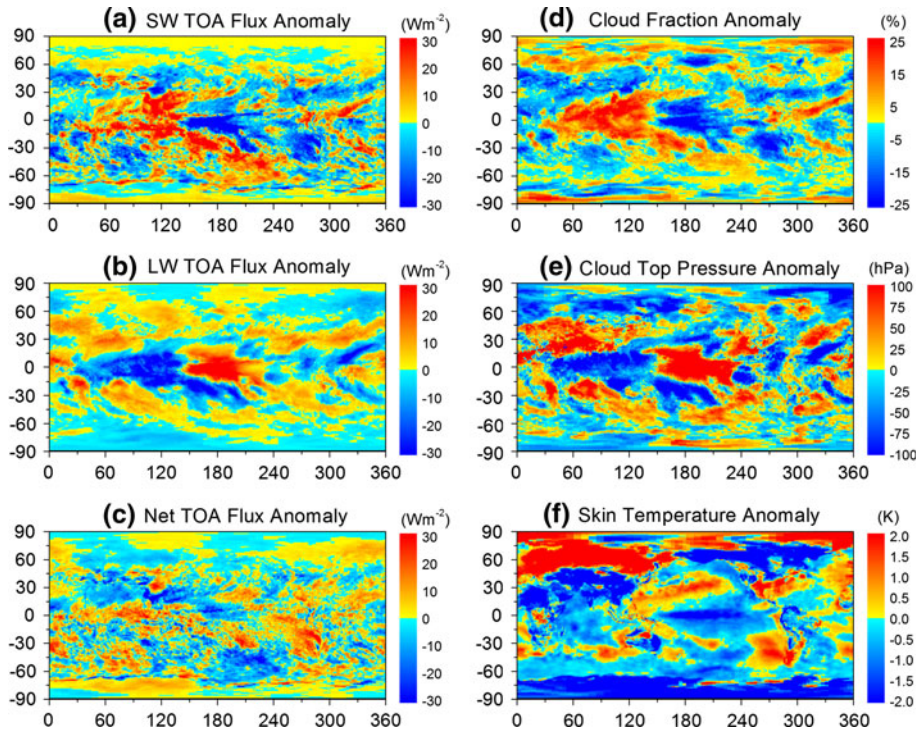


Fig. 10 Same as Fig. 9 but for February 2008

LW (negative SW) TOA flux anomalies occur over the Central equatorial Pacific Ocean. Consistent with this pattern, cloud fraction and cloud-top height increase to the west, while over the Central Pacific Ocean cloud fraction and cloud-top height decrease. The February 2008 pattern is consistent with expectation for a La Niña event. In January, the dipole pattern is much weaker. LW TOA flux anomalies over the Indian Ocean and Indonesia are positive, and over the Central Pacific Ocean, there is a mix of both weak positive and negative cloud fraction anomalies. This occurs in spite of the fact that January 2008 falls in the middle of the 06/2007–04/2009 La Niña event.

What happened to the convection over the Indian Ocean and Indonesia during January 2008? It turns out that, during January, this region corresponds to a period in which convection associated with the MJO was out of phase with La Niña-related convection. Gottschalk and Bell (2009) show that the 200-hPa velocity potential anomaly over this region is positive indicating upper-level convergence and suppressed convection. In contrast, during February, MJO and La Niña-related convection are in phase, resulting in intense convection. This interpretation and the CERES and MODIS results in Figs. 9 and 10 are corroborated by CALIPSO and Cloudsat observations of the difference between the cloud frequency of occurrence by altitude from 2008 and 2007 for January (Fig. 11a) and February (Fig. 11b) as a function of longitude across the Pacific Ocean between 0°S and 2.5°S. Results in Fig. 11 are from a merged satellite dataset that combines CALIPSO, Cloudsat, CERES and MODIS (C3M) (Kato et al. 2010). Negative anomalies in cloud frequency throughout the troposphere are seen between 90°E and 120°E in January 2008 compared to January 2007 (Fig. 11a). In February 2008, the convection reappears and

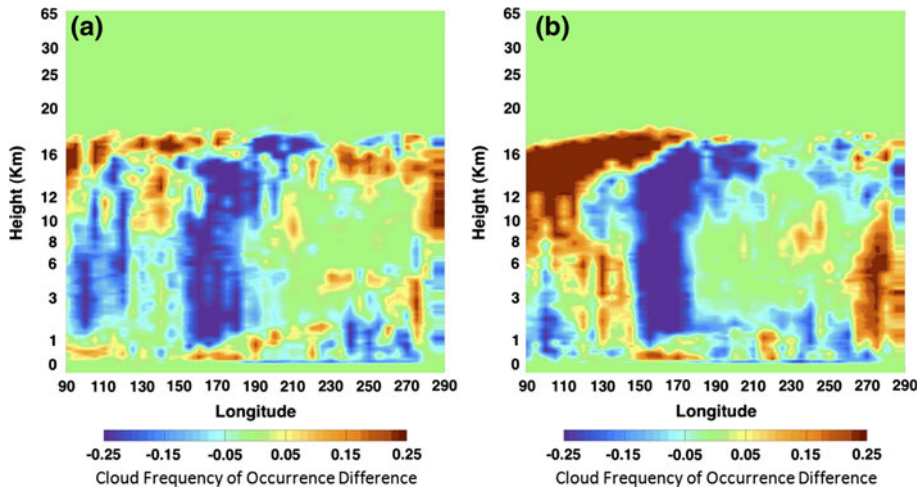


Fig. 11 Longitude-height cross-section of January 2008 minus January 2007 cloud frequency of occurrence difference for 0°S – 2.5°S : **a** January 2008 minus January 2007; **b** February 2008 minus February 2007

covers a large area contributing to strong negative SW and positive LW TOA flux anomalies (Fig. 10a, b). In both January and February, the negative difference in cloud frequency between 150°E , and the dateline is associated with the westward displacement of convection that is typical of La Niña events. This area coincides with negative cloud fraction anomalies in Figs. 9d and 10d.

4 Summary and Conclusions

There are now over a decade of cloud, aerosol, radiation and atmospheric state observations from advanced satellite instruments aboard the Terra and Aqua spacecrafts, and close to 5 years of vertical cloud and aerosol profile data from CloudSat and CALIPSO. These data provide a rich resource for studying ERB variations and the underlying processes. With the latest CERES calibration improvements, large-scale top-of-atmosphere (TOA) radiation changes during the past decade are observed to within 0.5 W m^{-2} per decade based upon comparisons between CERES Terra and Aqua, and between CERES and SeaWiFS, MODIS and AIRS. Monthly anomalies between the various datasets are highly correlated (coefficient of determination, r^2 , is generally >0.85).

The first decade of the Terra record was characterized by relatively modest La Niña and El Niño conditions during the first 7 years followed by prolonged strong La Niña conditions between June 2007 and April 2009, and a strong El Niño event immediately after. CERES outgoing LW radiation closely tracks with the Multivariate ENSO Index (MEI). During El Niño conditions outgoing LW flux increases, and decreases during La Niña conditions. Net incoming TOA flux was positive during the 2007–2009 La Niña conditions, primarily due to a pronounced decrease in outgoing LW TOA flux in the tropics in both cloud-free and all-sky conditions. This period also coincides with strong cooling and drying throughout the troposphere as captured by AIRS temperature profile data. Global outgoing LW TOA flux anomalies in late 2007/early 2008 are weaker than in the tropics due to compensation by clouds at middle latitudes: MODIS cloud fraction and MISR cloud-top height anomalies are both negative, resulting in positive middle latitude LW TOA flux anomalies.

Tropical anomalies in LW cloud radiative effect (CRE) are positive during La Niña events and negative during El Niño conditions. In the SW, cloud effects dominate by a factor of 3 over anomalies in clear-sky TOA flux. The net effect of clouds is to warm (cool) across the tropics during La Niña (El Niño). A striking feature is how different ENSO events are from one another.

The Terra, Aqua and other A-Train data provide excellent coverage of regional TOA flux and cloud property changes in response to atmosphere-ocean dynamics associated with ENSO and MJO events. The spatial and vertical distribution of clouds and radiation over the Indian Ocean and Indonesia when MJO convection is out of phase with La Nina convection in January 2008, and in phase in February 2008 is clearly captured by CERES, MODIS, CALIPSO and Cloudsat observations. Such dramatic events captured so clearly by these advanced instruments provides a wealth of new data for climate model evaluation and improvement.

While the new satellite instruments discussed in this study have clearly advanced the state-of-the-art in cloud-radiation observational capabilities, there is a critical need to extend the length of these records over multiple decades and further improve their accuracy in order to quantify how clouds are changing in a warmer climate and how cloud changes impact the Earth's radiation budget. One key observational requirement to address long-term climate change is an improvement in instrument calibration, particularly for the imager and radiation budget instruments. While the estimated stability of the CERES TOA radiation record of roughly 0.5 Wm^{-2} per decade is a factor of 3–4 better than anticipated prior to the launch of CERES, there is a need for another factor of 2–3 improvement in order to constrain cloud feedback.

Acknowledgments We thank the CERES science, algorithm and data management teams and the NASA Science Mission Directorate for supporting this research. CERES SSF1deg-lite_Ed2.5 data were obtained from http://ceres.larc.nasa.gov/compare_products.php. The NASA Langley Atmospheric Sciences Data Center processed the instantaneous Single Scanner Footprint data used to produce SSF1deg-lite_Ed2.5. We thank Drs. Mark Zelinka and Dennis Hartmann for sharing their perspectives on short-term cloud-radiation variability and cloud feedback. We thank Dr. Dale Walikainen for providing the results used in Fig. 17.

Open Access This article is distributed under the terms of the Creative Commons Attribution Noncommercial License which permits any noncommercial use, distribution, and reproduction in any medium, provided the original author(s) and source are credited.

Appendix 1: CERES Instrument Calibration Improvements

The primary purpose of an instrument's onboard calibration subsystem is to enable calibration scientists to detect, quantify and correct for changes in instrument sensitivity throughout the mission so that subtle changes in the climate system can be unambiguously detected. To ensure that ERB are accurate and consistent over the entire record, there is a need to periodically reprocess the entire record to account for instrument calibration drift too small to observe with a short record. The CERES team has recently conducted a major re-analysis of ground and in-flight calibration data and has implemented a new algorithm to characterize the spectral degradation of the CERES optics with time.

The two main quantities required in order to convert CERES detector output signals to unfiltered radiances are the instrument gain coefficients and spectral response functions. Both are determined prior to launch in a radiometric calibration facility. The primary in-

flight calibration system used to detect drifts in the CERES sensor gains is the Internal Calibration Module (ICM). ICM calibrations are performed on-orbit weekly to determine monthly gains. To reduce noise, a 5-month running mean is used. Recently, Shankar et al. (2010) re-evaluated the ground calibration data collected prior to CERES Terra and Aqua launches and derived new pre-launch calibration data. Thomas et al. (2010) summarize results of a reanalysis of CERES gain changes through March 2010.

Detecting in-orbit changes in spectral response function is more challenging as there are no onboard calibration sources that cover the entire spectral range observed by CERES. This is problematic as it is well established that instrument UV exposure and molecular contamination cause a loss of measurement sensitivity with time, particularly in the blue end of the solar spectrum (Clark and Dibattista 1978). Indeed, early analyses of the CERES SW data revealed significant decreases in albedo that were more pronounced for clear ocean scenes than cloudy scenes. Further, direct comparison of coincident CERES nadir radiances from CERES instrument pairs on both platforms were found to depend strongly on the instrument scan mode (Matthews et al. 2005). The primary mode of operation of CERES instruments is the crosstrack mode (i.e., perpendicular to the groundtrack), but CERES instruments can also be operated in a rotating azimuth plane mode (RAP), where the scan head rotates in azimuth as it scans in elevation. The direct comparison analyses showed that the degradation was more pronounced when the instruments were operated in RAP mode. This feature was subsequently used to derive Edition2 user-applied revisions to the RAP instrument for clear ocean and all-sky scenes. Subsequently analyses (Loeb et al. 2007) of SW fluxes showed a significant overall improvement for CERES Terra, but CERES Aqua still appeared to exhibit an artificial drift. In addition, the CERES team also found systematic daytime–nighttime LW TOA flux inconsistency.

TOA fluxes in CERES SSF1deg-lite_Ed2.5 are derived using a more comprehensive approach to correct for temporally varying spectral changes in SW and LW radiance measurements. Based upon data collected by prior missions, Matthews (2009) assumed the following expression for the loss of transmission with wavelength, or spectral degradation, in the SW:

$$\text{Tr}(\lambda) = 1 - Me^{-\alpha\lambda} \quad (1)$$

where M and α are coefficients of the fit to the data. Assuming Eq. 1 represents the shape of the change in spectral response, the direct comparison method can be used to infer wavelength-dependent changes in SW spectral response for each instrument pair on Terra and Aqua. We use $M = 1$ in Eq. 1, and derive an α value in each month of the Terra and Aqua missions by assuming spectral darkening in the SW only occurs for the instrument in RAP mode. The RAP instrument's α in a given month is selected from a set of candidate values to ensure that the ratio of unfiltered radiances (FM2/FM1 or FM3/FM4) for clear ocean scenes identified using the CERES cloud mask applied to MODIS radiances for 30°S and 30°N remains close to 1. The spectral darkening correction to the RAP instrument is thus only done relative to the crosstrack instrument. However, because modifying α changes the shape of the spectral response function (SRF), the current approach is wavelength dependent, thereby eliminating the need for separate scene-type-dependent correction factors. Spectral response functions (and associated spectral correction coefficients) for up to 83 α candidate values are considered in this procedure. Figure 12a–d show the spectral shape of the changes to the SRFs for each CERES instrument throughout the Terra and Aqua missions. Results for FM4 are available only from July 2002 through March 2005 due to an anomaly in the SW channel. FM2 and FM3 show the greatest spectral darkening because they have spent more time in RAP mode. Changes in spectral

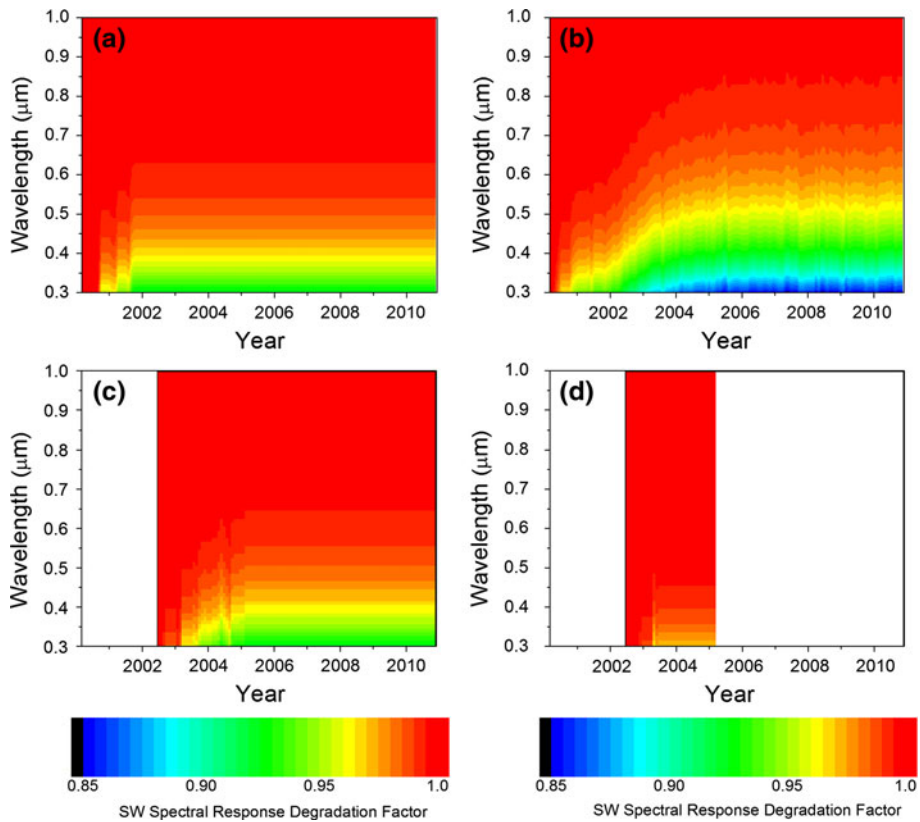


Fig. 12 SW spectral response degradation factor for **a** FM1, **b** FM2, **c** FM3, and **d** FM4

response reach 15% between 0.3 and 0.4 μm for FM2 and FM3, but remain <10% for FM1 and FM4.

Unfiltered CERES emitted LW radiances are determined directly from filtered total (TOT) channel measurements at night. Since the TOT channel radiance is comprised of both SW and LW contributions during daytime, unfiltered LW radiance is determined from TOT and SW filtered radiance measurements (Loeb et al. 2001). A drift in either the SW or LW portions of the TOT channel or in the SW channel can result in a drift in unfiltered LW radiance. Early validation of the CERES data showed a marked day–night bias with time in unfiltered LW radiance. This is illustrated in Fig. 13, which shows all-sky global mean daytime and nighttime LW TOA fluxes for FM1 Terra from the CERES Edition2 release. In Edition2, temporally varying gains are used, and there is also a correction in spectral response for the SW part of the TOT channel based upon a separate analysis using a 3-channel comparison with deep convective clouds. Unfortunately, because of the spectral difference between DCCs and all-sky radiances, adjustments to the SW part of the TOT based upon 3-channel consistency for DCCs does not translate to 3-channel consistency for all-sky. As a result, a trend of -2.7 Wm^{-2} per decade in day–night difference is observed for Edition2, which also affects the day/night average LW trend.

In order to quantify the drift in the SW portion of the TOT channel, Fig. 14 compares a time series of FM1 day–night LW TOA flux differences between 30°S and 30°N over ocean

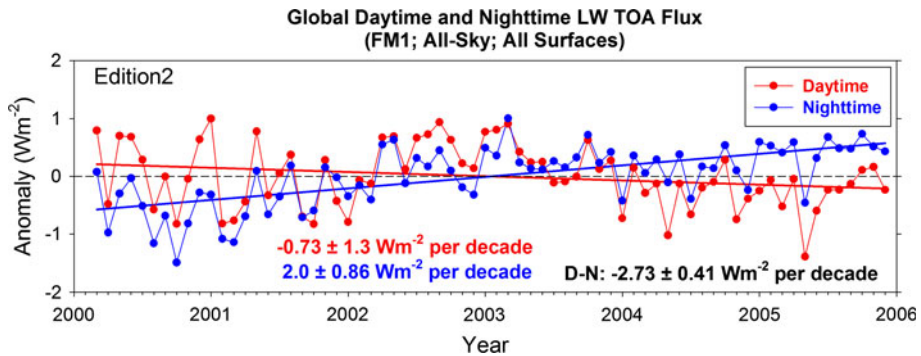


Fig. 13 All-sky global mean daytime and nighttime LW TOA flux anomalies for FM1 Terra from the CERES Edition2 release

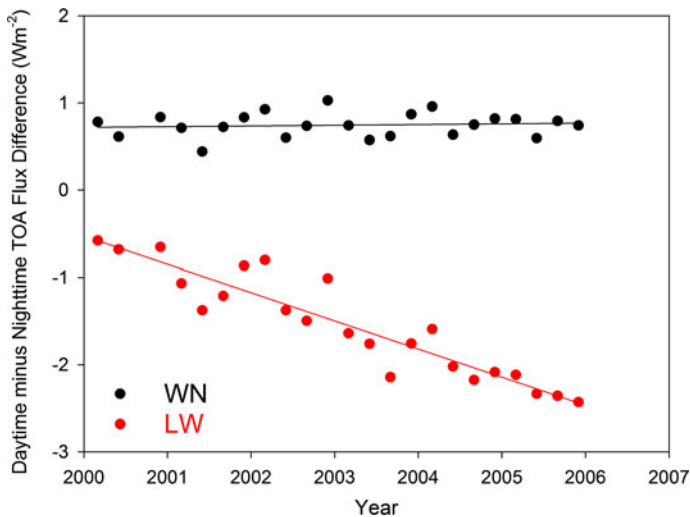


Fig. 14 FM1 day–night WN and LW TOA flux differences between 30°S and 30°N over ocean. For LW, the latest gains and SW spectral response function corrections are applied, but no change is made to the TOT spectral response function

after applying the latest gains and SW spectral response function correction with day–night TOA flux differences derived from WN channel radiances. The LW daytime–nighttime TOA flux differences show a decrease of 2 Wm^{-2} over 6 years, while WN day–night difference remain relatively constant. A 2 Wm^{-2} decrease in daytime–nighttime LW TOA flux difference exceeds expectation by an order-of-magnitude based upon observed temperature–humidity changes by AIRS level 2 data. Between 2002 and 2005, the change in the daytime–nighttime difference in temperature is $\approx 0.4 \text{ K}$ for layers above 10 hPa, which corresponds to a negligible TOA LW flux change. The change in water vapor mixing ratio is 0.05 g kg^{-1} below 700 hPa, corresponding to a 0.2 Wm^{-2} LW TOA flux change.

An alternate representation of the discrepancy between LW and WN day–night differences is provided in Fig. 15, which shows the relationship between 1° zonal average

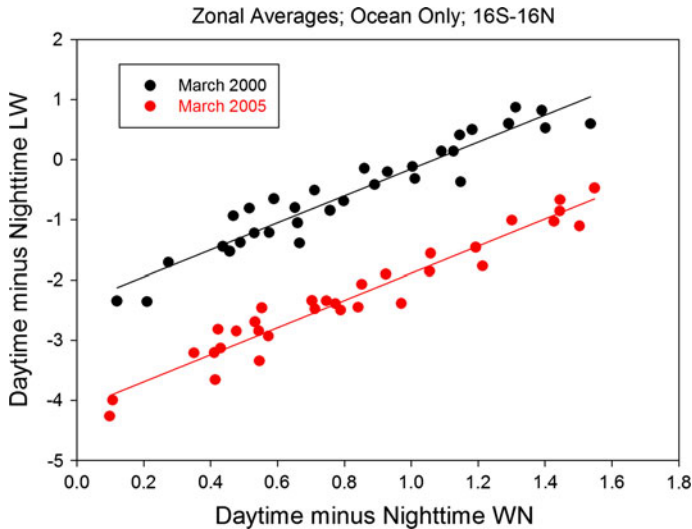


Fig. 15 Relationship between 1° zonal average LW and WN day–night unfiltered radiance differences from CERES FM1 for March 2000 and March 2005 over ocean between 16°S and 16°N

LW and WN day–night unfiltered radiance differences from CERES FM1 for March 2000 and March 2005 over ocean between 16°S and 16°N . While the slopes are the same for these 2 months, the March 2005 regression line is offset from that in March 2000. As an independent test of the temporal stability of the relationship between LW and WN daytime–nighttime TOA flux differences, we compared daytime–nighttime radiance differences for spectrally integrated AIRS radiances over the entire spectral range observed by AIRS and integrated AIRS radiances between 8.1 and $11.8\ \mu\text{m}$ (CERES WN channel) for 6 September months between 2002 and 2008 for tropical ocean scenes. We find that the daytime–nighttime radiance differences for these two spectral ranges are highly linear and repeatable from year-to-year, and the linear regression coefficients show no statistically significant changes for this period.

To compensate for the day–night drift in CERES LW unfiltered radiance, we adjust the SW portion of the TOT channel spectral response function to remove the offset from mission start in the day–night LW and WN regression relation. The adjustments to the SW portion of the TOT channel are derived for each month following the same approach as for the SW channel based upon Eq. 1. Figure 16a, b show deseasonalized daytime and nighttime LW TOA flux anomalies for 30°S – 30°N for the crosstrack CERES Aqua (Fig. 16a) and Terra (Fig. 16b) after adjusting the SW portion of the TOT spectral response function in each month. Daytime and nighttime LW TOA flux anomalies show consistent changes with no significant day–night drift.

Appendix 2: Reason for CERES Terra and Aqua LW Drift

Comparisons between CERES Terra and Aqua for July 2002–February 2010 (Table 1) show SW “trend” consistency of $0.04 \pm 0.27\ \text{Wm}^{-2}$ in the tropics and $0.12 \pm 0.25\ \text{Wm}^{-2}$ for the globe. In the LW, differences are much larger: the Terra minus Aqua difference is $-0.39 \pm 0.21\ \text{Wm}^{-2}$ for 30°S – 30°N , and for the globe, it is –

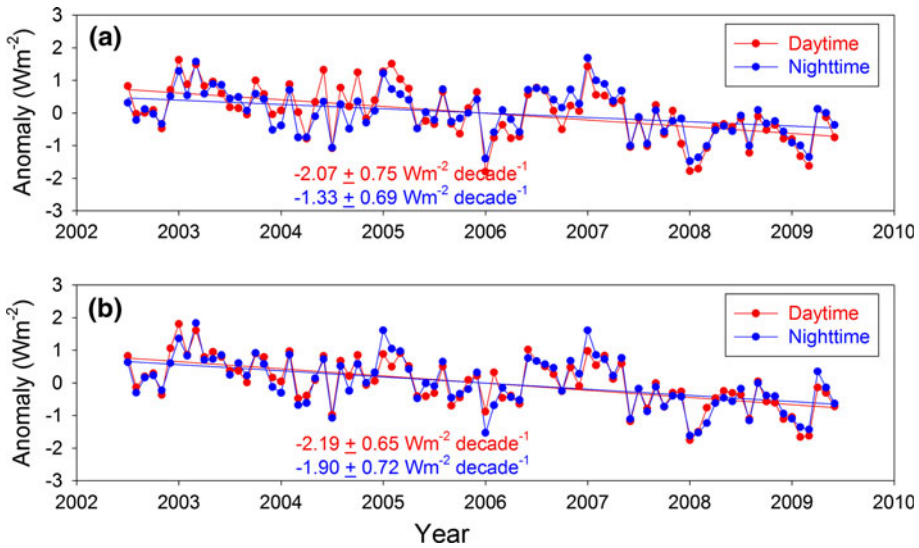


Fig. 16 Deseasonalized daytime and nighttime LW TOA flux anomalies for 30°S–30°N for crosstrack CERES **a** Aqua and **b** Terra after correcting for changes in SW and TOT channel spectral response function changes

$0.63 \pm 0.36 \text{ Wm}^{-2}$. This appendix provides an explanation why differences are so much larger in the LW.

To understand the cause of the LW discrepancy, it is helpful to consider some background information. Terra and Aqua carry two CERES instruments each. Early in both missions, one instrument on each spacecraft was placed in crosstrack mode to optimize spatial sampling, and the other instrument was either in a rotating azimuth plane (RAP) scan mode or alongtrack (AT) mode. Only crosstrack CERES data are used in producing Level-3 gridded data products because crosstrack provides global coverage daily. CERES RAP data are used to optimize angular sampling in order to construct CERES angular distribution models, and CERES AT data are used for validating the CERES angular models. To ensure the gimbals on each instrument were fully exercised, each instrument's scan mode was alternated from RAP to crosstrack and back on a 3-month cycle during the first 2 years of Terra and first year of Aqua. Eventually, FM1 on Terra and FM4 on Aqua were permanently placed in crosstrack mode, and FM2 and FM3 in RAP/AT mode. It was later realized that operating the instruments in RAP mode exposes the optics to increased UV exposure and molecular contamination. Preventative measures were taken by restricting the instruments from scanning in the RAM direction.

Both CERES instruments on Terra have been functioning nominally since the beginning of the mission in December 1999. With the exception of 10 months (04/00; 08/00–10/00; 02/01–04/01; 08/01–10/01; 01/06–02/06), FM1 has been in crosstrack mode throughout the Terra mission. Unfortunately, the SW channel of CERES FM4 on Aqua failed in March 2005. Consequently, with the exception of 6 months (11/02–01/03; 05/03–07/03), FM4 was the main crosstrack instrument from July 2002–March 2005, and FM3 has been in crosstrack mode from April 2005 onwards. The CERES team placed all 4 CERES instruments (FM1–FM4) on the same radiometric scale at their respective beginning of missions (Szewczyk et al. 2011). A one-time adjustment to FM2 was applied to match FM1 in March of 2000. Similarly, adjustments to FM3 and FM4 were made in July 2002 to match FM1. All-sky

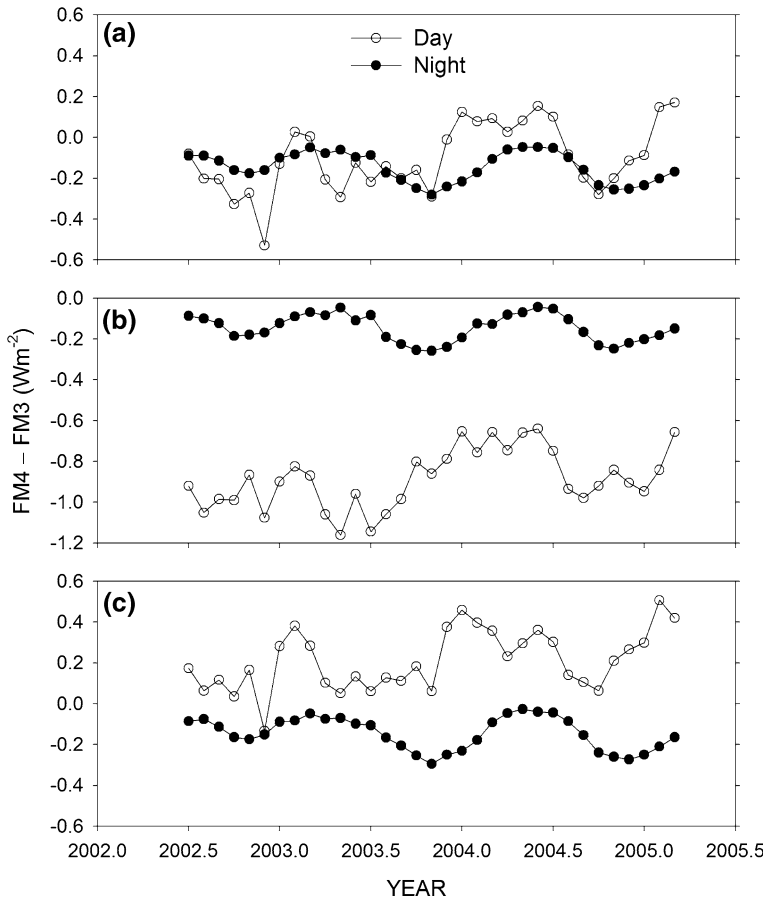


Fig. 17 Mean difference between FM4 and FM3 coincident nadir LW footprint pairs for all-sky conditions during daytime and nighttime for **a** all surfaces; **b** land only and **c** ocean only

data over all surface types were used to derive the radiometric scale adjustments. Each instrument is fully autonomous after that without any further corrections.

As a check for any discontinuities in the transition between FM4 and FM3, TOA fluxes from the two CERES instruments on Aqua are directly compared with one another at nadir over the exact same area and at the same time. Figure 17a shows FM3 and FM4 LW direct comparison results during nighttime and daytime for all-sky conditions over all surface types. At night, the FM4–FM3 difference at the beginning of the mission is -0.1 Wm^{-2} and grows to -0.2 Wm^{-2} by March 2005. Because of this difference, continuing the FM4 record with FM3 in April 2005 introduces a spurious 0.2 Wm^{-2} increase in the middle of the record, which contributes to the negative slope in the Terra minus Aqua anomaly difference. During daytime, FM4 and FM3 are closer to one another at the time of the FM4 to FM3 transition, but this is largely due to compensation between land and ocean, as shown in Fig. 17b, c, which provide FM4–FM3 direct comparison results for land and ocean, respectively. During daytime, the FM3 LW TOA flux exceeds FM4 by $\approx 0.8 \text{ Wm}^{-2}$ over land/desert (Fig. 17b), while FM3 is lower than FM4 by $\approx 0.3 \text{ Wm}^{-2}$ over ocean (Fig. 17c).

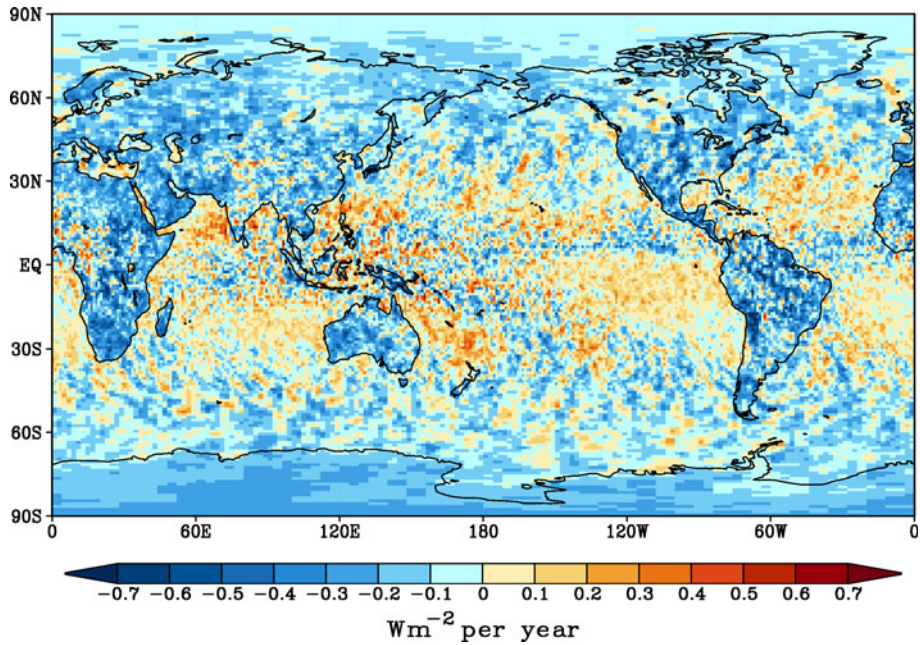


Fig. 18 Slope of Terra minus Aqua all-sky LW TOA flux anomalies for July 2002–June 2009 from SSF1deg-lite_Ed2.5 (units: Wm^{-2} per year)

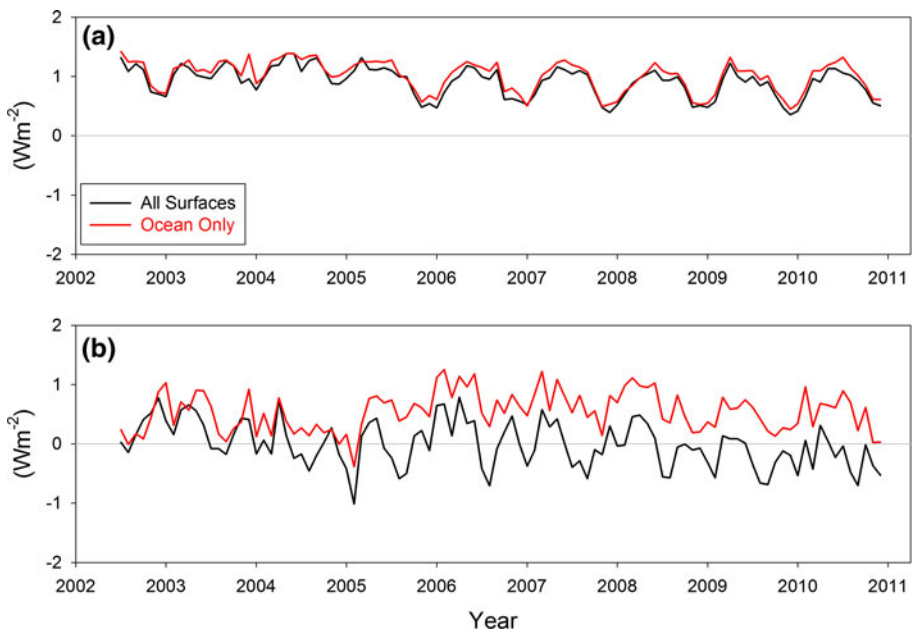


Fig. 19 Terra minus Aqua all-sky LW TOA flux difference over 60°S–60°N for **a** nighttime and **b** daytime based on the SSF1deg-lite_Ed2.5 product

These marked discontinuities between FM3 and FM4 cause large regional differences between Terra and Aqua anomalies. Figure 18 shows a regional map of the slope of Terra minus Aqua all-sky LW TOA flux anomaly difference from the CERES SSF1deg-lite_Ed2.5 data product. Consistent with results in Fig. 17a–c, the slope is negative over land and is mostly positive over ocean. An alternate representation is provided in Fig. 19a, b, which shows Terra minus Aqua all-sky LW TOA flux differences for 60°S–60°N at night (Fig. 19a) and during daytime (Fig. 19b). At night, Terra LW TOA fluxes exceed Aqua fluxes by $\approx 1 \text{ Wm}^{-2}$ for both ocean and all surface types, whereas the daytime results depend on surface type. There is also a noticeable jump in the ocean-only LW TOA flux difference (red line in Fig. 19b) in spring 2005 at the time when the Aqua crosstrack instrument transitions from FM4 to FM3.

The CERES team is currently developing an improved approach for placing FM3 and FM4 on the same radiometric scale that removes the large scene-type inconsistencies found in Figs. 17, 18, and 19. The CERES team anticipates reprocessing the Aqua record with this improvement in a future release.

References

- Allan RP, Slingo A (2002) Can current climate model forcings explain the spatial and temporal signatures of decadal OLR variations? *Geophys Res Lett* 29(7):1141–1144
- Barnes WL, Pagano TS, Salomonson VV (1998) Prelaunch characteristics of the moderate resolution imaging spectroradiometer (MODIS) on EOS-AM1. *IEEE Trans Geosci Remote Sens* 36:1088–1100
- Clark LG, Dibattista JD (1978) Space qualification of optical-instruments using NASA long duration exposure facility. *Opt Eng* 17:547–552
- Clement AC, Burgman R, Norris JR (2009) Observational and model evidence for positive low-level cloud feedback. *Science* 325:460–464
- Dessler AE (2010) A determination of the cloud feedback from climate variations over the past decade. *Science* 330(6010):1523–1527. doi:[10.1126/science.1192546](https://doi.org/10.1126/science.1192546)
- Di Girolamo L, Menzies A, Zhao G, Mueller K, Moroney C, Diner DJ (2010) Multi-angle imaging spectroradiometer (MISR) level 3 cloud fraction by altitude algorithm theoretical basis. JPL D-62358, Jet Propulsion Laboratory, Pasadena, 23 pp. Available from: http://eosps.gsfc.nasa.gov/eos_home_page/for_scientists/atbd/docs/MISR/MISR_CFBA_ATBD.pdf
- Doelling DR, Keyes DF, Rutan DA, Nordeen ML, Morstad D, Sun M, Loeb NG, Wielicki BA, Young DF (2012) Geostationary enhanced temporal interpolation for CERES flux products. *J Appl Meteor Climatol* (submitted)
- Eitzen ZA, Xu K-M, Wong T (2011) An estimate of low-cloud feedbacks from variations of cloud radiative and physical properties with sea surface temperature on interannual time scales. *J Clim* 24:1106–1121
- Fu Q, Liou K-N (1992) On the correlated-k distribution method for radiative transfer in nonhomogenous atmospheres. *J Atmos Sci* 49:2139–2156
- Fu Q, Liou K-N (1993) Parameterization of the radiative properties of cirrus clouds. *J Atmos Sci* 50:2008–2025
- Gottschalk J, Bell GD (2009) The Madden–Julian oscillation. *Bull Am Meteorol Soc* 90:S78–S79
- Hartmann DL, Larson K (2002) An important constraint on tropical cloud-climate feedback. *Geophys Res Lett* 29:1951. doi:[10.1029/2002GL015835](https://doi.org/10.1029/2002GL015835)
- Hooker SB, Esaias WE, Feldman GC, Gregg WW, McClain CR (1992) An overview of SeaWiFS and ocean color. *SeaWiFS Tech. Rep. Series*, vol 1, NASA Tech. Memo. 104566, 785 pp
- Kato S, Sun-Mack S, Miller WF, Rose FG, Chen Y, Minnis P, Wielicki BA (2010) Relationships among cloud occurrence frequency, overlap, and effective thickness derived from CALIPSO and CloudSat merged cloud vertical profiles. *J Geophys Res* 115:D00H28. doi:[10.1029/2009JD012277](https://doi.org/10.1029/2009JD012277)
- L'Ecuyer TS, Jiang JH (2010) Touring the atmosphere aboard the A-Train. *Phys Today* 63:36–41
- Lin B, Wielicki B, Chambers L, Hu Y, Xu K-M (2002) The Iris hypothesis: a negative or positive cloud feedback? *J Clim* 15:3–7
- Loeb NG, Kato S, Loukachine K, Manalo-Smith N (2005) Angular distribution models for top-of-atmosphere radiative flux estimation from the clouds and the earth's radiant energy system instrument on the Terra satellite. Part I: methodology. *J Atmos Oceanic Technol* 22:338–351

- Loeb NG, Priestley KJ, Kratz DP, Geier EB, Green RN, Wielicki BA, Hinton POR, Nolan SK (2001) Determination of unfiltered radiances from the clouds and the earth's radiant energy system (CERES) instrument. *J Appl Meteorol* 40:822–835
- Loeb NG et al (2007) Multi-instrument comparison of top-of-atmosphere reflected solar radiation. *J Clim* 20:575–591
- Loeb NG, Wielicki BA, Doelling DR, Smith GL, Keyes DF, Kato S, Manalo-Smith N, Wong T (2009) Toward optimal closure of the Earth's top-of-atmosphere radiation budget. *J Clim* 22:748–766
- Madden RA, Julian PR (1971) Detection of a 40–50 day oscillation in the zonal wind in the tropical Pacific. *J Atmos Sci* 28:702–708
- Madden RA, Julian PR (1994) Observations of the 40–50 day tropical oscillation: a review. *Mon Weather Rev* 122:814–837
- Matthews (2009) In-flight spectral characterization and calibration stability estimates for the clouds and the earth's radiant energy system (CERES). *J Atmos Ocean Tech* 26:1685–1716
- Matthews G, Priestley KJ, Spence P, Cooper D, Walikanen D (2005) Compensation for spectral darkening of short wave optics occurring on the cloud's and the earth's radiant energy system. In: Butler JJ (ed) *Earth observing systems X, Proceedings of SPIE*, vol 5882. SPIE, Bellingham, doi: [10.1117/12.618972](https://doi.org/10.1117/12.618972)
- Minnis P, Sun-Mack S, Young DF, Heck PW, Garber DP, Chen Y, Spangenberg DA, Arduini RF, Trepte QZ, Smith WL Jr, Ayers JK, Gibson SC, Miller WF, Chakrapani V, Takano Y, Liou KN, Xie Y (2011) CERES edition-2 cloud property retrievals using TRMM VIRS and Terra and Aqua MODIS data, part I: algorithms. *IEEE Trans Geosci Remote Sens* 49:4374–4400
- Philander SGH (1990) *El Niño, La Niña and the southern oscillation*. Academic Press, San Diego
- Remer LA et al (2005) The MODIS aerosol algorithm, products and validation. *J Atmos Sci* 62:947–973. doi:[10.1175/JAS3385.1](https://doi.org/10.1175/JAS3385.1)
- Salomonson VV, Barnes WL, Maymon PW, Montgomery HE, Ostrow H (1989) MODIS: advanced facility instrument for studies of the earth as a system. *IEEE Trans Geosci Remote Sens* 27:145–153
- Shankar MS, Thomas S, Priestley KJ (2010, Aug) Pre-launch characterization of spectral response functions for the clouds and earth's radiant energy system (CERES) instrument sensors. In: *Proceedings of SPIE, earth observing systems XV*, vol 7807, 780702
- Suarez MJ (2005) Documentation and validation of the Goddard earth observing system (GEOS) data assimilation system—version 4, vol 26. Tech. Rep. Series on Global Modeling and Data Assimilation, NASA/TM-2005-104606, 181 p
- Susskind J, Molnar G, Iredell L, Loeb NG (2012) Interannual variability in outgoing longwave radiation as observed by AIRS and CERES. *J Geophys Res* (submitted)
- Szewczyk ZP, Priestley KJ, Walikainen DR, Loeb NG, Smith GL (2011) Putting all CERES Scanners (Terra/Aqua) on the same Radiometric Scale. In: *Remote sensing of clouds and atmosphere*, vol XIII, *Proceedings of SPIE, Paper ERS11-RS04-5*
- Thomas S, Priestley KJ, Manalo-Smith N, Loeb NG, Hess PC, Shankar M, Walikainen DR, Szewczyk ZP, Wilson RS, Cooper DL (2010, Aug) Characterization of the clouds and the earth's radiant energy system (CERES) sensors on the Terra and Aqua spacecraft. In: *Proceedings of SPIE, earth observing systems XV*, vol 7807, 780702
- Trenberth KE, Fasullo JT, O'Dell C, Wong T (2010) Relationships between tropical sea surface temperature and top-of-atmosphere radiation. *Geophys Res Lett* 37:L03702
- Wielicki BA et al (2002) Evidence for large decadal variability in the tropical mean radiative energy budget. *Science* 295:841–844
- Wolter K, Timlin MS (1998) Measuring the strength of ENSO events: how does 1997/1998 rank? *Weather* 53:315–324
- Wong T, Wielicki BA, Lee RB III, Smith GL, Bush KA, Willis JK (2006) Reexamination of the observed decadal variability of the earth radiation budget using altitude-corrected ERBE/ERBS nonscanner WFOV data. *J Clim* 19:4028–4040
- Woods T, Rottman G, Harder J, Lawrence G, McClintock B, Kopp G, Pankratz C (2000) Overview of the EOS SORE mission. *SPIE Proc* 4135:192–203
- Xue Y, Reynolds RW (2009) Sea surface temperatures in 2008. *Bull Am Meteorol Soc* 90:S47–S48
- Young DF, Minnis P, Doelling DR, Gibson GG, Wong T (1998) Temporal interpolation methods for the clouds and the earth's radiant energy system (CERES) experiment. *J Appl Meteorol* 37:572–590
- Zelinka MD, Hartmann DL (2010) Why is longwave cloud feedback positive? *J Geophys Res* 115:D16117. doi:[10.1029/2010JD013817](https://doi.org/10.1029/2010JD013817)
- Zelinka MD, Hartmann DL (2011) The observed sensitivity of high clouds to mean surface temperature anomalies in the tropics. *J Geophys Res* 116:D23103. doi:[10.1029/2011JD016459](https://doi.org/10.1029/2011JD016459)